

Quantum-corrected semiclassical theory for strong-field ionization

Wenhai Xie ¹, Min Li ^{1,*}, Yueming Zhou,¹ and Peixiang Lu^{1,2}

¹Wuhan National Laboratory for Optoelectronics and School of Physics,
Huazhong University of Science and Technology, Wuhan 430074, China

²Optics Valley Laboratory, Hubei 430074, China



(Received 13 March 2023; revised 30 May 2023; accepted 2 November 2023; published 4 December 2023)

We develop a quantum-corrected semiclassical approach to study the strong-field ionization of an atom. In this approach, the electron wave packet is propagated using Bohmian trajectories near the center of the Coulomb potential and a Herman-Kluk propagator away from the center of the Coulomb potential. We employ this approach to calculate the photoelectron momentum distributions from tunneling and multiphoton ionization of an atom in strong laser fields. The results agree well with the numerical solutions of the time-dependent Schrödinger equation. By selecting electrons released within one laser cycle, we remove the intercycle interference structure from the photoelectron momentum distributions and study the sub-laser-cycle electron dynamics. We show that the subcycle temporal information of the electron obtained by the quantum-corrected semiclassical approach is consistent with the quasiclassical result in the tunneling ionization regime, while it differs from the quasiclassical result in the multiphoton ionization regime. Furthermore, using a semiclassical backpropagation based on the Herman-Kluk propagator, we obtain the information of the ionized wave packets near the tunnel exit and compare them with the quasiclassical results.

DOI: [10.1103/PhysRevA.108.063102](https://doi.org/10.1103/PhysRevA.108.063102)

I. INTRODUCTION

Atoms or molecules can be ionized in a strong laser pulse, leading to many highly nonlinear phenomena, such as above-threshold ionization (ATI) [1], high-order harmonic generation [2,3], and nonsequential double ionization [4,5]. According to the Keldysh-Faisal-Reiss (KFR) theory [6], two ionization regimes can be distinguished by the Keldysh parameter $\gamma = \omega\sqrt{2I_p}/E_0$, where I_p is the ionization potential, E_0 is the field amplitude, and ω is the laser frequency. In general, the tunneling ionization is dominated when $\gamma \ll 1$, while the multiphoton ionization prevails when $\gamma \gg 1$.

Over the past decades, both tunneling and multiphoton ionizations of atoms and molecules have been intensively studied experimentally as well as theoretically. Various theoretical approaches have been developed. As the workhorse of strong-field physics, strong-field approximation (SFA) [7,8] was widely used, which does not account for the effect of the excited bound states and the effect of the electron-ion interaction in the continuum. However, both effects are found to be particularly important to reproduce the experimental results [9,10]. Generally, the numerical solution of the time-dependent Schrödinger equation (TDSE) is the most accurate approach. However, the TDSE approach cannot provide clear physical pictures for the strong-field phenomena of interest and requires too much computing resource. Compared to the TDSE method, the classical or quasiclassical simulations show numerical simplicity and allow us to identify the mechanism underlying the strong-field phenomena

in terms of classical trajectories [11–18]. These classical or quasiclassical simulations include the classical-trajectory Monte Carlo simulations [12], the quantum-trajectory Monte Carlo method [16,17], the Coulomb-corrected SFA (CCSFA) [13–15], which corrects the trajectories from the SFA theory by accounting for the Coulomb field perturbatively, the Coulomb quantum-orbit SFA [18], and so on. In those simulations, the classical trajectories start to propagate from the position of the tunnel exit. Consequently, those classical and quasiclassical models rely on the assumption of tunneling, which precludes the applicability of those models to the multiphoton ionization regime [19]. Moreover, it is still controversial how the initial conditions of the electron trajectories should be specified, i.e., the tunnel time, the position of the tunnel exit and the initial velocity of the electron [20–24]. It was found that the final electron momentum distribution depends sensitively on these initial conditions [20,25,26]. Besides, those classical trajectories ignored the quantum nature of the tunneling ionization. Some studies used Bohmian trajectories to consider the effect of the quantum potential on the electron [27–29]. However, it is difficult to obtain a convergent result for quantum interference using the Bohmian trajectories.

Alternatively, a semiclassical propagator, developed by Herman and Kluk [30–32], can also be used to investigate the strong-field ionization. The Herman-Kluk (HK) propagator is a semiclassical approximation of the quantum propagator, involving real-valued classical trajectory [33–35]. Compared to the classical and quasiclassical approaches, the HK propagator has considered the quantum effect and thus it is more accurate. More importantly, it can be employed in both tunneling and multiphoton ionization regimes, providing an

*mli@hust.edu.cn

alternative perspective of the electron dynamics during strong-field ionization. Previously, the HK propagator was employed to investigate the problem of tunneling [36–38]. It was also used in studying high-harmonic generation and strong-field ionization [39–42]. However, those methods based on the HK propagator cannot yield a quantitative agreement with the full quantum result, e.g., TDSE. The main reason is that the HK propagator is based on a semiclassical approximation to the full Feynman path integral, which is only exact for a quadratic potential [30]. For the Coulomb potential of a real atom, the electron dynamics predicted by the HK propagator strongly differ from those of the TDSE, especially near the center of the Coulomb potential.

In this paper, we develop an approach based on the HK propagator to study strong-field ionization. We propagate the electron wave packet using the Bohmian trajectories near the center of the Coulomb potential and the semiclassical HK propagator away from the center of the Coulomb potential. This approach is referred to as quantum-corrected semiclassical (QCS) theory in this paper. We employ this approach to calculate the photoelectron momentum distributions in the tunneling ionization regime with an 800-nm laser field and the multiphoton ionization regime with a 400-nm laser field. The results agree well with the TDSE. Using the QCS method, we also study the subcycle electron dynamics and obtain the information of the electron at near the tunnel exit.

This paper is organized as follows. In Sec. II, the theoretical methods are described, and the transformation from the Bohmian trajectory to the semiclassical HK propagation is shown. In Sec. III, a comparison of the QCS model with the TDSE as well as the CCSFA is presented. Finally, we give a brief summary of the paper in Sec. IV. Atomic units (a.u.) are used throughout unless specified otherwise.

II. THEORETICAL APPROACH

A. Time-dependent Schrödinger equation

To investigate the ionization of atoms in a strong laser field, we numerically solve the two-dimensional TDSE of an Ar atom with the single-active-electron approximation. In the length gauge, the TDSE reads as

$$i \frac{\partial}{\partial t} \psi(\mathbf{r}, t) = \left[-\frac{\nabla^2}{2} + V(\mathbf{r}) + \mathbf{r} \cdot \mathbf{E}(t) \right] \psi(\mathbf{r}, t), \quad (1)$$

where $\psi(\mathbf{r}, t)$ is the time-dependent wave function in coordinate space. The Coulomb interaction between the electron and the ion is approximated by a soft-core potential $V(\mathbf{r}) = -1/\sqrt{r^2 + a^2}$ with $a = 0.624$ to match the ionization potential of the Ar atom. $\mathbf{E}(t)$ is the laser electric field.

The split-operator spectral method [43] on a Cartesian grid is used to numerically solve the two-dimensional TDSE. The Cartesian grid ranges from -450 a.u. to 450 a.u. for each dimension with a grid spacing of 0.22 a.u. The initial wave function is prepared by imaginary-time propagation [44]. In our simulation, the time step of the propagation is $\Delta t = 0.0441$ a.u. For each 100 time steps, we split the electron wave function into two parts,

$$\begin{aligned} \psi(\mathbf{r}, \tau_i) &= M_s(r, R_b) \psi(\mathbf{r}, \tau_i) + [1 - M_s(r, R_b)] \psi(\mathbf{r}, \tau_i) \\ &= \psi_{\text{inner}}(\mathbf{r}, \tau_i) + \psi_{\text{outer}}(\mathbf{r}, \tau_i), \end{aligned} \quad (2)$$

where $M_s(r, R_b) = 1 - 1/(1 + e^{-(r-R_b)/\Delta})$ is the absorption function [45] that separates the propagation space into inner and outer regions smoothly. In the present simulation, we choose $R_b = 150$ a.u. and $\Delta = 8.0$ a.u. The wave function in the inner region is propagated under the full Hamiltonian numerically, while in the outer region, the wave function is projected to momentum space,

$$D(\mathbf{p}, \tau_i) = \int \frac{e^{-i[\mathbf{p} + \mathbf{A}(\tau_i)] \cdot \mathbf{r}}}{2\pi} \psi_{\text{outer}}(\mathbf{r}, \tau_i) d^2r. \quad (3)$$

Here, $\mathbf{A}(t)$ is the vector potential of the laser field. Then we propagate $D(\mathbf{p}, \tau_i)$ to the end of the pulse using the Volkov propagator [46],

$$D^f(\mathbf{p}, \tau_i) = e^{-i \int_{\tau_i}^{t_f} \frac{1}{2} [\mathbf{p} + \mathbf{A}(t)]^2 dt} D(\mathbf{p}, \tau_i), \quad (4)$$

where t_f is the end of the propagation time. Finally, we obtain the photoelectron momentum distribution (PMD) by

$$\frac{dP(\mathbf{p})}{dE d\theta} = \left| \sum_{\tau_i} D^f(\mathbf{p}, \tau_i) \right|^2. \quad (5)$$

Here, $E = p^2/2$ is the electron energy and θ is the angle of the emitted electron.

B. Quantum-corrected semiclassical theory

The QCS theory is based on the Bohmian trajectories and the semiclassical Herman-Kluk propagator. Before formulating the QCS theory, we briefly describe the concepts of Bohmian trajectories and semiclassical HK propagator.

1. Bohmian trajectories

In Bohmian mechanics [47], the wave function is replaced by an ensemble of particles. Unlike in quantum mechanics, which is determined by the TDSE, i.e., Eq. (1), those Bohmian trajectories are describe by the Hamilton-Jacobi equation and the continuity equation [47]. In principle, Bohmian mechanics is equivalent to quantum mechanics. Compared with the classical trajectory, the Bohmian trajectory includes the effect of a nonlocal quantum potential and follows the current of the probability density. In fact, Bohmian trajectories can be obtained through the time-dependent wave function in the TDSE, instead of solving the Hamilton-Jacobi equation [27,28]. As the wave function $\psi(\mathbf{r}, t)$ evolves with time, the Bohmian trajectories are propagated by solving the equation of motion,

$$\frac{d\mathbf{r}_j(t)}{dt} = \mathbf{v}[\mathbf{r}_j(t), t]. \quad (6)$$

Here, j is the index of each Bohmian trajectory. The velocity of the particle in Eq. (6) is given by

$$\mathbf{v} = \nabla \Phi = \text{Im} \frac{\nabla \psi}{\psi} \quad (7)$$

in the length gauge. Here, Φ is the phase of the wave function ψ . After initial discretization of the probability density into a set of particles, a certain amount of probability within a volume element $ds_j(t)$, i.e., the trajectory weight, is associated with each trajectory. At the limit of $ds_j \rightarrow 0$, the weight

of each Bohmian trajectory assigned at the initial time is conserved over the time evolution [48,49].

2. Semiclassical Herman-Kluk propagator

To obtain the wave function at time t , in addition to the direct solution of the TDSE in Eq. (1), we can write it as an integral over the initial wave function

$$\psi(\mathbf{r}, t) = \int d\mathbf{r}' K(\mathbf{r}, \mathbf{r}', t, 0) \psi_i(\mathbf{r}'), \quad (8)$$

where $K(\mathbf{r}, \mathbf{r}', t, 0)$ is the full quantum propagator. Physically, $K(\mathbf{r}, \mathbf{r}', t, 0)$ describes the amplitude for a transition from the point described by coordinates \mathbf{r}' at time 0 to the point described by coordinates \mathbf{r} at time t . Following the work by Herman and Kluk [30], the quantum propagator is replaced with the semiclassical approximation by

$$K^{\text{HK}}(\mathbf{r}, \mathbf{r}', t, 0) = \frac{1}{(2\pi)^N} \int d\mathbf{p} \int d\mathbf{q} C(\mathbf{p}, \mathbf{q}, t, 0) \times e^{iS(\mathbf{p}, \mathbf{q}, t, 0)} \langle \mathbf{r} | \mathbf{p}_t \mathbf{q}_t \gamma_2 \rangle \langle \mathbf{p} \mathbf{q} \gamma_1 | \mathbf{r}' \rangle. \quad (9)$$

Here, $(\mathbf{p}_t, \mathbf{q}_t)$ is the phase space point at time t that evolves classically from the initial phase space point (\mathbf{p}, \mathbf{q}) . N is the dimension of the system. The classical action S along the trajectory is

$$S(\mathbf{p}, \mathbf{q}, t, 0) = \int_0^t d\tau [\mathbf{p}_t \cdot \dot{\mathbf{q}}_\tau - H(\mathbf{p}_\tau, \mathbf{q}_\tau, \tau)]. \quad (10)$$

Here, H is the Hamiltonian of the system. The coherent state wave packet $|\mathbf{p} \mathbf{q} \gamma\rangle$ with average position \mathbf{q} and momentum \mathbf{p} takes the form

$$\langle \mathbf{r} | \mathbf{p} \mathbf{q} \gamma \rangle = \left(\frac{2\gamma}{\pi} \right)^{N/4} \exp[-\gamma(\mathbf{r} - \mathbf{q})^2 + i\mathbf{p}(\mathbf{r} - \mathbf{q})]. \quad (11)$$

γ is the width parameter of the coherent state. The prefactor $C(\mathbf{p}, \mathbf{q}, t, 0)$ is defined by

$$C(\mathbf{p}, \mathbf{q}, t, 0) = \left(\frac{\pi}{2} \right)^{N/2} (\gamma_1 \gamma_2)^{-N/4} \times \left| \frac{1}{2\pi i} \left[-\frac{\partial \mathbf{p}_t}{\partial \mathbf{q}} + 2i\gamma_2 \frac{\partial \mathbf{q}_t}{\partial \mathbf{q}} - 2i\gamma_1 \left(-\frac{\partial \mathbf{p}_t}{\partial \mathbf{p}} + 2i\gamma_2 \frac{\partial \mathbf{q}_t}{\partial \mathbf{p}} \right) \right] \right|^{1/2}. \quad (12)$$

The branch of the square root is chosen so that $C(\mathbf{p}, \mathbf{q}, t, 0)$ is a continuous function of time for $t > 0$. The four time-dependent factors in Eq. (12) can be obtained by numerically integrating the following differential equations [35]:

$$\begin{aligned} \frac{d}{dt} \left(\frac{\partial p_{ti}}{\partial z_j} \right) &= - \sum_{k=1}^N \left(\frac{\partial^2 H}{\partial p_{tk} \partial q_{ti}} \frac{\partial p_{tk}}{\partial z_j} + \frac{\partial^2 H}{\partial q_{tk} \partial q_{ti}} \frac{\partial q_{tk}}{\partial z_j} \right), \\ \frac{d}{dt} \left(\frac{\partial q_{ti}}{\partial z_j} \right) &= \sum_{k=1}^N \left(\frac{\partial^2 H}{\partial p_{tk} \partial p_{ti}} \frac{\partial p_{tk}}{\partial z_j} + \frac{\partial^2 H}{\partial q_{tk} \partial p_{ti}} \frac{\partial q_{tk}}{\partial z_j} \right), \end{aligned} \quad (13)$$

where $z = p$ or q . Then, the propagation of the initial wave function can be approximated by

$$\psi^{\text{HK}}(\mathbf{r}, t) = \frac{1}{(2\pi)^N} \int d\mathbf{p} \int d\mathbf{q} C(\mathbf{p}, \mathbf{q}, t, 0) \times e^{iS(\mathbf{p}, \mathbf{q}, t, 0)} \langle \mathbf{r} | \mathbf{p}_t \mathbf{q}_t \gamma_2 \rangle \langle \mathbf{p} \mathbf{q} \gamma_1 | \psi_i \rangle. \quad (14)$$

The HK propagator can be thought of as an expansion in an overcomplete set of coherent state wave packets. The centers of the coherent state wave packets follow classical trajectories up to time t , at which point the coherent state wave packets are summed up to reconstruct the propagator. For the original HK propagator, the width parameter is set to be unchanged during the classical propagation, i.e., $\gamma_1 = \gamma_2$, which is also known as the frozen Gaussian approximation [30–32]. Subsequently, it was shown that these Gaussian widths can differ from each other to better reflect the characteristic sizes of the initial and final wave functions [42]. Overlaps of the $|\mathbf{p}_t \mathbf{q}_t \gamma_1\rangle$ to the $|\mathbf{p}_t \mathbf{q}_t \gamma_2\rangle$ basis are included in the prefactor $C(\mathbf{p}, \mathbf{q}, t, 0)$ [34]. In contrast to the familiar Van Vleck–Gutzwiller (VVG) expression [50], the HK expression describes the propagator in terms of classical trajectories obeying certain initial conditions. Thus, the difficult and time-consuming search process needed to determine special trajectories obeying double-ended boundary conditions can be avoided in the HK propagator. The HK propagator is more convenient to establish the classical-quantum correspondence as compared to other semiclassical methods.

3. Quantum correction to the semiclassical propagator

Since the HK propagator is only exact for the quadratic potentials, the wave functions calculated by the semiclassical HK propagator for the Coulomb potential would deviate from the exact solution of TDSE, especially near the origin of the Coulomb potential. For strong-field ionization, the ionized electron is influenced by both laser and Coulomb fields. Frequently, the binding potential can be taken as a perturbation as compared to the laser field at the position sufficiently far away from the atomic core, and the binding potential itself can also be expanded to Taylor series up to second order, with small higher-order terms disregarded. Thus, the semiclassical HK propagator is only accurate far away from the core. In contrast, around the center of the core, the electron-ion interaction dominates over the influence of the laser field. For this case, the ionic Coulomb potential cannot be approximated by a quadratic potential. The electron dynamics near the atomic core should be described by the full quantum propagation.

The QCS method we developed relies on the separation of the coordinate space into inner and outer regions, as shown in Fig. 1. The evolution of the electron in the inner region is calculated by Bohmian trajectories. In the outer region, the semiclassical HK propagator is used to describe the electron dynamics. Note that the idea of partitioning the space and treating each partition separately is similar to the analytical R-matrix method [51].

In our quantum-corrected semiclassical theory, we first replace the position \mathbf{q} of the initial phase space in Eq. (14) with the position \mathbf{r}_j of the Bohmian trajectory at any propagation

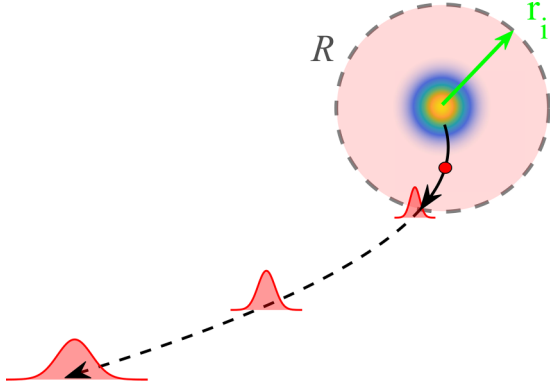


FIG. 1. Illustration of the quantum-corrected semiclassical approach. Inside the transformation boundary R with a radius r_i (gray dashed circle), the electron wave function is propagated using the Bohmian trajectories. The Bohmian trajectories are transformed to a set of Gaussian wave packets when they reach the transformation boundary and are subsequently calculated using the semiclassical HK propagator in the outer region.

time t'_p ,

$$\begin{aligned} \psi^{\text{HK}}(\mathbf{r}, t) = & \frac{1}{(2\pi)^N} \sum_j ds_j(t'_p) \int d\mathbf{p} C(\mathbf{p}, \mathbf{r}_j, t, t'_p) \\ & \times e^{iS(\mathbf{p}, \mathbf{r}_j, t, t'_p)} \langle \mathbf{r} | \mathbf{p}_t \mathbf{q}_t \gamma_2 \rangle \langle \mathbf{p}_j \gamma_1 | \psi(t'_p) \rangle. \end{aligned} \quad (15)$$

This equation can be understood in the following way. Each Bohmian trajectory is transformed to a bunch of Gaussian wave packets in the momentum space at the same time t'_p , which is similar to the picture of optical diffraction in the spirit of Huygens' principle. After the transformation, the Gaussian wave packets evolve classically with a phase accumulated along the classical trajectories. For strong-field ionization, we can replace the electron wave function with the Bohmian trajectories. The Bohmian trajectories are affected by both the classical and quantum potential, which are a full quantum propagation. When the Bohmian trajectories reach the boundary R , which is far from the parent core that the ionic potential could be approximated by a quadratic potential, we transform the corresponding Bohmian trajectories to a bunch of Gaussian wave packets in the momentum space. After that, the Gaussian wave packets evolve the same way as the semiclassical HK propagation. Finally, the ionized electron wave function can be written as

$$\begin{aligned} \psi^{\text{HK}}(\mathbf{r}, t_f) = & \frac{1}{(2\pi)^N} \sum_j ds_j(t_j^c) \int d\mathbf{p} C(\mathbf{p}, \mathbf{R}_j, t_f, t_j^c) \\ & \times e^{iS(\mathbf{p}, \mathbf{R}_j, t_f, t_j^c)} \langle \mathbf{r} | \mathbf{p}_{t_f} \mathbf{q}_{t_f} \gamma_2 \rangle \\ & \times \langle \mathbf{p} \mathbf{R}_j \gamma_1 | \psi(t_j^c) \rangle, \end{aligned} \quad (16)$$

where t_j^c is the time that the j th Bohmian trajectory crossed the boundary. \mathbf{R}_j is the corresponding crossing position on the boundary. The summation only includes these Bohmian trajectories that can reach the boundary R , namely, the ionized Bohmian trajectories.

The volume element $ds_j(t_j^c)$ in Eq. (16) can also be written as

$$ds_j(t_j^c) = v_{\perp}(t_j^c) dR d\tau. \quad (17)$$

v_{\perp} is the normal component of the local velocity perpendicular to the boundary at the crossing position. dR is the corresponding element on the boundary R and $d\tau$ is the crossing time element. Substituting Eq. (17) into Eq. (16) and using the continuity of the volume elements, Eq. (16) can be rewritten as

$$\begin{aligned} \psi^{\text{HK}}_{\text{ion}}(\mathbf{r}, t_f) = & \frac{1}{(2\pi)^N} \oint_R dR \int_0^{t_f} d\tau \int d\mathbf{p} v_{\perp}(\mathbf{R}, \tau) \\ & \times C(\mathbf{p}, \mathbf{R}, t_f, \tau) e^{iS(\mathbf{p}, \mathbf{R}, t_f, \tau)} \\ & \times \langle \mathbf{r} | \mathbf{p}_{t_f} \mathbf{q}_{t_f} \gamma_2 \rangle \langle \mathbf{p} \mathbf{R} \gamma_1 | \psi(\tau) \rangle. \end{aligned} \quad (18)$$

The first integral is over the boundary R . Based on Eq. (18), we only need to calculate the local velocity and the projection of the wave function onto the Gaussian wave packets on the boundary along the propagation time τ to obtain the final ionized electron wave function. Using the momentum representation of the final Gaussian wave packets, we can obtain the final ionized electron wave function in the momentum space

$$\begin{aligned} \psi^{\text{HK}}_{\text{ion}}(\mathbf{p}', t_f) = & \frac{1}{(2\pi)^N} \oint_R dR \int_0^{t_f} d\tau \int d\mathbf{p} v_{\perp}(\mathbf{R}, \tau) \\ & \times C(\mathbf{p}, \mathbf{R}, t_f, \tau) e^{iS(\mathbf{p}, \mathbf{R}, t_f, \tau)} \\ & \times \langle \mathbf{p}' | \mathbf{p}_f \mathbf{q}_f \gamma_2 \rangle \langle \mathbf{p} \mathbf{R} \gamma_1 | \psi(\tau) \rangle, \end{aligned} \quad (19)$$

which is the main result of this approach. Note that v_{\perp} is the velocity of the Bohmian particle perpendicular to the transformation boundary. Thus, the Bohmian trajectories are involved in Eq. (19). Actually, we did not solve the Hamilton-Jacobi equation or TDSE to obtain the Bohmian trajectories in the inner region. Instead, we use the numerical solutions of the TDSE to obtain the local velocity of the Bohmian trajectory on the boundary according to Eq. (7) and then transform the Bohmian trajectory to a set of Gaussian wave packets according to Eq. (19). Though the Bohmian trajectories are not actually calculated in this model, the derivation of Eq. (19) relies on the concept of the Bohmian trajectories as described above.

We implement the QCS in a two-dimensional space, similar to the above TDSE, and the time-dependent wave function $\psi(\tau)$ in Eq. (19) is provided by the TDSE. At the end of the propagation time, we select the Gaussian wave packets with central positions and momenta corresponding to positive energies. In order to obtain the final photoelectron momentum distribution, we also replace the central momenta of the Gaussian wave packets at the end of the propagation time with the asymptotic momenta derived from Kepler's laws [52]. In the present work, we set the radius of the transformation boundary as $r_i = 20$ a.u., and we have checked that the obtained results are independent of the radius r_i in the vicinity of 20 a.u. The initial Gaussian width γ_1 is set to be 0.02, while the final Gaussian width $\gamma_2 = \gamma_1/30$. Since the second partial derivative of the ionic potential with respect to position is so small in the outer region, the prefactor in Eq. (12) can be simplified to $C(\mathbf{p}, \mathbf{R}, t_f, \tau) = \frac{1}{2}(\gamma_1 \gamma_2)^{-1/2} [\gamma_2 + \gamma_1 - 2i\gamma_1 \gamma_2 (t_f - \tau)]$.

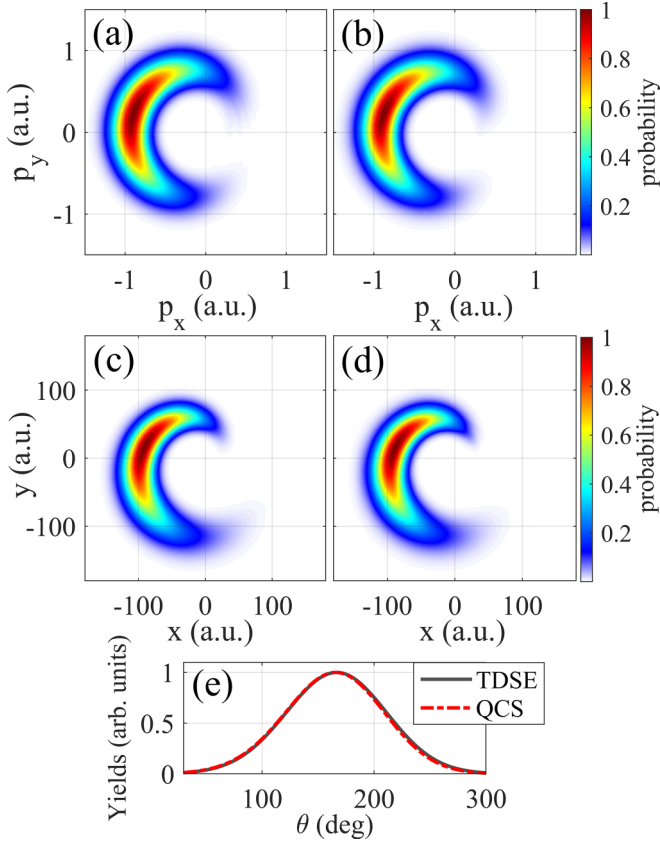


FIG. 2. (a and b) PMDs and (c and d) wave-function probability distributions at the end of a two-cycle circularly polarized laser pulse for the laser intensity $I = 1.4 \times 10^{14}$ W/cm². The laser wavelength is 800 nm. (a) and (c) are the TDSE results and (b) and (d) are obtained from the QCS. (e) The angular distributions of the PMDs from TDSE (gray solid line) and QCS (red dash-dotted line).

III. RESULTS AND DISCUSSION

We first use the QCS theory to study atomic ionization by a strong circularly polarized few-cycle laser field, which is widely used for theoretical study of the attoclock [53–56]. The electric field $\mathbf{E}(t) = -d\mathbf{A}/dt$ of the laser pulse can be obtained from the vector potential

$$\mathbf{A}(t) = A_0 \sin^4(\omega t/2n)[\cos(\omega_{800}t)\mathbf{e}_x - \sin(\omega_{800}t)\mathbf{e}_y]. \quad (20)$$

Here, ω_{800} is the frequency of an 800-nm field. The pulse length is parametrized with the number of optical cycles n . \mathbf{A} vanishes for $|t - t_c| > nT/2$, where $t_c = nT/2$ corresponds to the pulse center and $T = 2\pi/\omega_{800}$ is the laser field period. In Figs. 2(a) and 2(b) we show the PMDs calculated by the TDSE and QCS in a two-cycle ($n = 2$) circularly polarized laser pulse at the laser intensity of $I = 1.4 \times 10^{14}$ W/cm². One can see that the PMDs are identical for those two approaches, both of which did not show clear interference patterns. The angular distributions of the PMDs using those two approaches are shown in Fig. 2(e), which also coincide with each other. In Figs. 2(c) and 2(d) we show the probability distributions of the ionized wave functions at the instant corresponding to the end of the laser field. The result from the QCS is also identical to that from the TDSE. Thus, the QCS approach is accurate for the case of few-cycle circularly polarized laser fields.

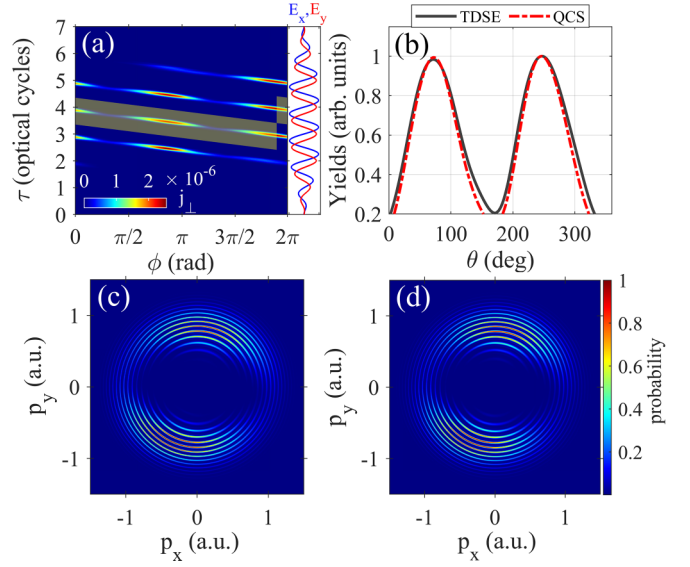


FIG. 3. (a) The distribution of the perpendicular probability flux j_{\perp} on the boundary along the propagation time in the 800-nm laser field (left side) and the corresponding electric field (right side). ϕ is the polar angle on the transformation boundary. The shadow area shows the ionization within a single laser cycle. (b) The angular distributions of the PMDs calculated by the TDSE (gray solid line) and QCS (red dash-dotted line). (c and d) The PMDs calculated by the TDSE (c) and QCS (d) in a seven-cycle elliptically polarized laser field with the intensity of $I = 1.4 \times 10^{14}$ W/cm². The laser wavelength is 800 nm and the ellipticity is 0.85.

Next, we consider the case of an elliptically polarized multicycle 800-nm laser field, where the quantum interference becomes important. The electric field of the elliptically polarized laser field is given by

$$\mathbf{E}(t) = E_0 f_1(t)[\sin(\omega_{800}t)\mathbf{e}_x + \epsilon \cos(\omega_{800}t)\mathbf{e}_y]. \quad (21)$$

Here, the ellipticity of the pulse ϵ is set to be 0.85. E_0 is chosen to be 0.0481 a.u. corresponding to an intensity of 1.4×10^{14} W/cm². $f_1(t)$ is a trapezoidal envelope which has seven optical cycles in total with two cycles ramping on and off. In order to see how the Bohmian trajectories cross the boundary in this multicycle laser field, we show the distribution of the perpendicular probability flux j_{\perp} on the boundary along the propagation time in Fig. 3(a). One can clearly see several periodic peaks on the distribution, which correspond to the ionized wave packets in the strong 800-nm laser field. The calculated PMDs using the TDSE and QCS are shown in Figs. 3(c) and 3(d). The result from the QCS model agrees with that from the TDSE. More importantly, the QCS can reproduce the quantum interference structures of the ionized wave packets in the PMD, i.e., the ATI rings in Figs. 3(c) and 3(d), which is difficult to implement using the Bohmian trajectory method. The angular distributions of the PMDs from the TDSE and QCS methods, as shown in Fig. 3(b), also agree with each other.

In the above 800-nm laser field, tunneling ionization is dominated. In the following, we validate our QCS theory in the multiphoton ionization regime. To this end, we use an elliptically polarized multicycle 400-nm laser field. The electric

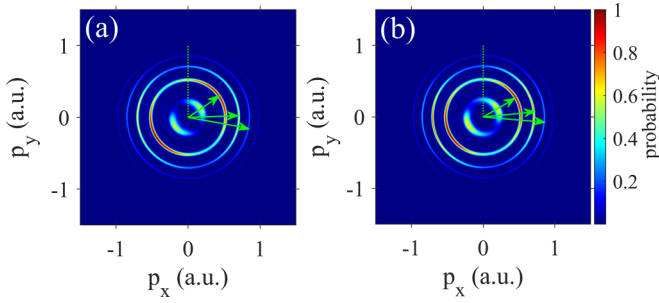


FIG. 4. The PMDs calculated by the (a) TDSE and (b) QCS in the 400-nm laser field with the intensity of $I = 1.4 \times 10^{14}$ W/cm². The maxima of the PMDs for the second to fourth orders of the ATI are indicated by the green arrows.

field is given by

$$\mathbf{E}(t) = E_0 f_2(t) [\sin(\omega_{400} t) \mathbf{e}_x + \epsilon \cos(\omega_{400} t) \mathbf{e}_y]. \quad (22)$$

The ellipticity of the pulse and the laser intensity are the same as the 800-nm laser field. This corresponds to a Keldysh parameter of 2.55 for the atom, indicating that multiphoton ionization dominates under these conditions. $f_2(t)$ is a trapezoidal envelope which has ten optical cycles in total with three cycles ramping on and off. The PMDs calculated by the TDSE and QCS methods are shown in Figs. 4(a) and 4(b). Again, the result predicted by QCS theory resembles the full quantum calculation. The QCS can also reproduce the ATI rings in the TDSE. Previously, the attoclock experiment has been extended to the case of the 400-nm laser field [57,58]. It was found that the angular offset with respect to the minor axis increases with the electron energy. In Figs. 4(a) and 4(b), one can clearly see the same trend for the offset angle in the PMDs calculated by the TDSE as well as the QCS theory.

Because the QCS is a trajectory-based method, we can study the electron dynamics within one laser cycle using the QCS method. To this end, we only select those trajectories that cross the transformation boundary within a time interval of one cycle of the laser field, as shown by the shadow area in Fig. 3(a). Consequently, the intercycle interference patterns [59] can be removed from the PMDs. In Figs. 5(a) and 5(b), we show the single-cycle ionized PMDs for the 800-nm and 400-nm laser fields. The remaining interference patterns in Figs. 5(a) and 5(b) are due to the quantum interference of the electron wave packets at the beginning and the end of the selected time window in Fig. 3(a). One can observe that the single-cycle ionized PMD for the 400-nm laser field shows a larger angular offset than that for the 800-nm laser field, which mainly comes from a larger Coulomb effect in the 400-nm laser field. Meanwhile, the ionized wave packets are less distinguishable from each other for the 400-nm laser field. To compare the QCS theory with previous trajectory-based quasiclassical models, we also employ the CCSFA model [15] to calculate the single-cycle ionization for the 800-nm and 400-nm laser field, as shown in Figs. 5(c) and 5(d). One can see that the result from the QCS qualitatively agrees with the CCSFA result for the 800-nm laser field, as shown in Figs. 5(a) and 5(c). However, for the 400-nm laser field, the PMD calculated by the CCSFA differs significantly from that of the QCS. Particularly, the angular offset in the PMD cal-

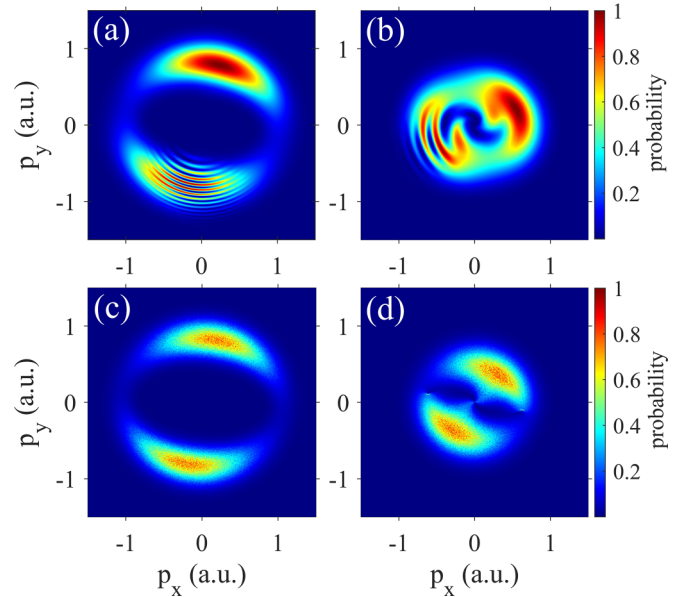


FIG. 5. PMDs calculated by the (a and b) QCS and (c and d) CCSFA by selecting the electrons released within a single cycle. (a) and (c) are the results in the 800-nm laser field and (b) and (d) are the results in the 400-nm laser field.

culated by the CCSFA is clearly smaller than the QCS result, as shown in Figs. 5(b) and 5(d). This is because the CCSFA model ignores many wavelike properties of the electron, e.g., diffraction, during the wave packet propagation, though a phase is encoded in each trajectory. As a result, the CCSFA method is less accurate in the multiphoton ionization regime.

The QCS theory involves real-valued classical trajectories in the outer region, which allows us to study the subcycle ionization dynamics. In the CCSFA, each point on the PMD is linked to one trajectory released at a specific ionization time, establishing a time-to-momentum mapping relation. However, the QCS theory is based on an approximation to the Feynman path integral. There are many trajectories corresponding to each point on the PMD. Thus, in the QCS model, the time is not a deterministic number, but a probability distribution. Since all the real-valued trajectories in the QCS are born on the transformation boundary, we use this beginning time to explore the ionization dynamics in the following. According to Eq. (19), the ionization amplitude for final momentum \mathbf{p}' can be written as

$$\psi_{\text{ion}}^{\text{HK}}(\mathbf{p}', t_f) = \int_0^{t_f} F(\mathbf{p}', \tau_b) d\tau_b. \quad (23)$$

Here, τ_b is the time when the Bohmian trajectories arrive at the boundary. τ_b is referred to as crossing time in this paper. $F(\mathbf{p}', \tau_b)$ is the crossing time probability amplitude, which is given by

$$F(\mathbf{p}', \tau_a) = \frac{1}{(2\pi)^N} \oint_{\mathcal{R}} d\mathbf{R} \int d\mathbf{p}_{\perp}(\mathbf{R}, \tau_b) \times C(\mathbf{p}, \mathbf{R}, t_f, \tau_b) e^{iS(\mathbf{p}, \mathbf{R}, t_f, \tau_b)} \times \langle \mathbf{p}' | \mathbf{p}'_f \mathbf{q}_f \gamma_2 \rangle \langle \mathbf{p} \mathbf{R} \gamma_1 | \psi(\tau_b) \rangle, \quad (24)$$

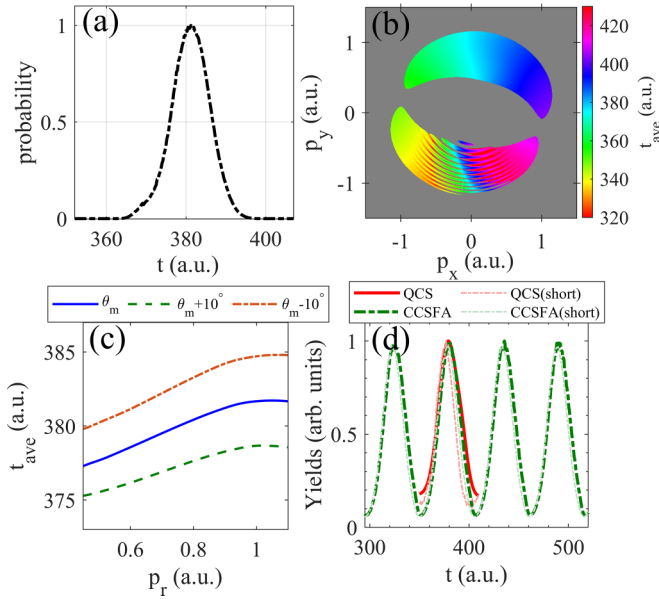


FIG. 6. (a) The distribution of the crossing time at the transformation boundary for the peak of the PMD in an 800-nm laser field. (b) The momentum-resolved average crossing time spectrum. (c) The average crossing time as a function of the radial momentum for several emission angles. (d) The average crossing time distributions calculated by the QCS (red solid line) and CCSFA (green dash-dotted line). The dashed lines with light color in (d) shows the average crossing time distributions calculated by the short-range Yukawa potential.

where \mathbf{p}'_f is the asymptotic momentum of the final momentum. In Fig. 6(a), we show the crossing time probability distribution $|F|^2$ for the peak of the PMD in Fig. 5(a) in the 800-nm laser field. One can see that the crossing time distribution is similar to a Gaussian distribution with a width of around 10 a.u., reflecting the quantum property of the QCS theory. In some previous studies, the Feynman path integral was employed to explore the problem of the tunneling time [60–64]. It is found that the tunneling time also shows a probability distribution. Similar to that case, we define a complex-valued average time as

$$\langle \tau_b \rangle = \frac{\int_0^\infty \tau_b F(\mathbf{p}', \tau_b) d\tau_b}{\int_0^\infty F(\mathbf{p}', \tau_b) d\tau_b}. \quad (25)$$

We find that the imaginary part of this average time is negligible. Thus, we next discuss the real part of the average time.

Figure 6(b) shows the momentum-resolved average crossing time spectrum calculated from the single-cycle ionization of the 800-nm laser field. One can see that the average crossing time increases along the clockwise direction, i.e., the rotating direction of the elliptical electric field, consistent with the principle of the attosecond angular streaking [53,65]. In Fig. 6(c), we show the average crossing time as a function of the radial momentum for momentum angle of θ_m , $\theta_m + 10^\circ$, and $\theta_m - 10^\circ$. θ_m is the angle of the peak of the PMD in Fig. 5(a). The average crossing time increases with the magnitude of the radial momentum, indicating that the electron with higher energy crosses the boundary later. In Fig. 7, we show the result of the 400-nm laser field. The crossing time

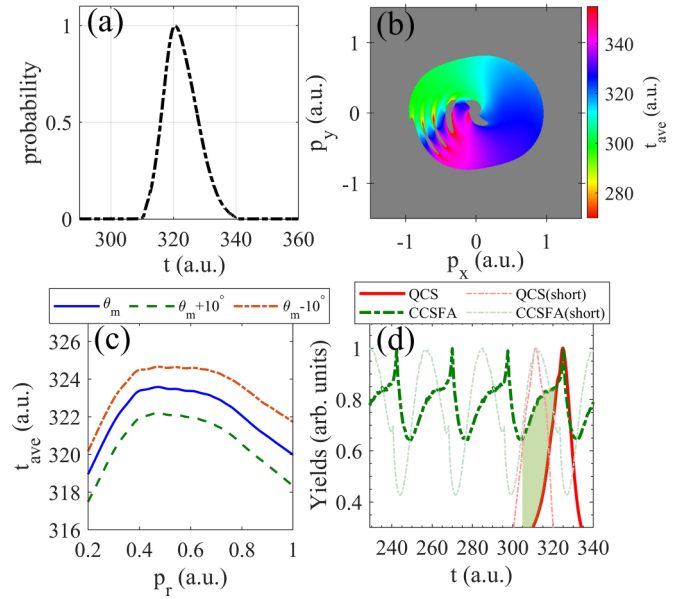


FIG. 7. The same as Fig. 6 but for a 400-nm laser field. The shadow area in (d) shows the difference of the average crossing time distribution between the QCS and CCSFA methods.

distribution of the peak of the PMD also shows a width of around 10 a.u., as shown in Fig. 7(a). The momentum-resolved average crossing time spectrum calculated from the single-cycle ionization of the 400-nm laser field is shown in Fig. 7(b). The average crossing time also increases along the rotating direction of the 400-nm elliptical electric field, which is similar to the case of the 800-nm laser field. However, the average crossing time as a function of the radial momentum, shown in Fig. 7(c), is different from that of the 800-nm laser field. The average crossing time increases with the radial momentum at the low-energy region ($p_r < 0.4$ a.u.), while it decreases with the radial momentum for the high-energy region ($p_r > 0.4$ a.u.). This means that, at $p_r > 0.4$ a.u., the electron with lower energy has a smaller offset angle, which is consistent with Fig. 4.

Using the QCS theory, we can achieve a momentum-to-time mapping according to the average crossing time. In Fig. 6(d), we show the calculated average crossing time distribution by the QCS in the 800-nm laser field, in comparison with the result by the CCSFA. In the CCSFA, the crossing time corresponds to the instant when the classical trajectories arrive at the transformation boundary R . One can see that the result from the QCS agrees closely with that from the CCSFA. The average crossing time distribution in the 400-nm laser field is shown in Fig. 7(d). Compared to the QCS result, there are more electrons released at an earlier time in the CCSFA method, as shown by the shaded area in Fig. 7(d), which indicates that the electrons in the CCSFA simulation reach the boundary earlier than those in the QCS. Since the electron-ion interaction mainly occurs in the inner region, compared to the QCS, the electrons in the CCSFA experience a shorter interaction time and thus the ionic potential has a smaller influence on the electrons. As a result, a smaller angular shift appears in the CCSFA simulation, as compared to the QCS method. For comparison, we also show the average crossing

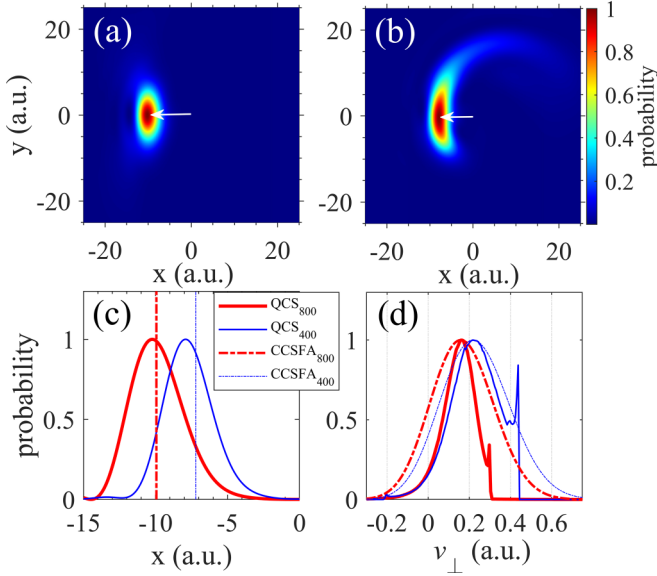


FIG. 8. (a and b) The wave-function probability distributions at the peak of the electric field for the (a) 800-nm and (b) 400-nm laser fields obtained by the QCS model. The instantaneous tunneling direction is indicated by the white arrows. (c) The wave-function probability distribution along the tunneling direction for the 800-nm (red thick line) and 400-nm laser (blue thin line) fields. The vertical dashed lines show the positions of tunnel exit calculated by the CCSFA for the peaks of the PMDs. (d) The transverse velocity distributions at the instant of the laser-field peak extracted from the QCS (solid lines) and CCSFA (dashed lines).

time distributions for the short-range Yukawa potential [53] in Figs. 6(d) and 7(d). One can see that the result from the QCS agrees with that from the CCSFA when the Coulomb tail is screened. There is also a clear time shift between the results of the Coulomb potential and the short-range potential in the 400-nm laser field, while the time shift becomes small for the case of the 800-nm laser field. That indicates a larger influence of electron-ion interaction in the 400-nm laser field than the case of the 800-nm laser field.

To further study the electron dynamics near the tunneling exit, we propagate the ionized electron wave packet backwards to the instant of the laser-field peak t_p , at which the electron location is very close to the tunnel exit position. Thus, we can obtain the information of the electron near the tunnel exit position using the QCS method. This backpropagation method is similar to that used in Ref. [54], but it is based on the HK propagator. Note that the HK propagator can still be used near the tunnel exit position if the backpropagated wave packet spends a short time around the ionic core. The ionized electron wave function at time t_p can be written as

$$\begin{aligned} \psi_{\text{ion}}^{\text{HK}}(\mathbf{r}, t_p) &= \frac{1}{(2\pi)^N} \oint_{\mathbf{R}} d\mathbf{R} \int_0^{t_f} d\tau \int d\mathbf{p} v_{\perp}(\mathbf{R}, \tau) \\ &\times C(\mathbf{p}, \mathbf{R}, t_p, \tau) e^{iS(\mathbf{p}, \mathbf{R}, t_p, \tau)} \\ &\times \langle \mathbf{r} | \mathbf{p}_p, \mathbf{q}_p \rangle_2 \langle \mathbf{p} \mathbf{R} | \gamma_1 | \psi(\tau) \rangle. \end{aligned} \quad (26)$$

Here, we only backpropagate those trajectories that released within one half laser cycle. In Figs. 8(a) and 8(b), we show the wave-function probability distributions at the peak of the

electric field for the 800-nm and 400-nm laser fields. One can see that the ionized wave packet for the 800-nm laser field at t_p is symmetric about the x axis, i.e., the tunneling direction, as shown in Fig. 8(a). However, the ionized wave packet for the 400-nm laser field reveals a long tail in the upper half plane. This tail is related to the low-energy electrons of the PMD in Fig. 5(b).

A cut along the $-x$ direction of Figs. 8(a) and 8(b) is shown in Fig. 8(c). One can see that at the peak of the electric field, the electron starts to propagate from some positions which are very close to the tunnel exit. The most probable position for the 400-nm laser field is closer to the nucleus than that for the 800-nm laser field. For comparison, we also show the positions of the tunnel exit obtained by the CCSFA by the vertical dashed lines. In the CCSFA, the tunnel exit for the 400-nm laser field is also closer to the nucleus than that of the 800-nm laser field. This is because of the stronger nonadiabatic effect in the 400-nm laser field [57]. The most probable release position calculated by the QCS agrees qualitatively with the tunnel exit position calculated by the CCSFA. However, one can still see a comparably large difference between those two methods, especially for the case of the 400-nm laser field. This reflects a stronger wave nature of the electron wave packet propagation for the 400-nm field, which was ignored in the CCSFA method. Moreover, we can obtain the transverse velocity of the ionized electron at the peak of the electric field by calculating the local velocity $v_{\perp} = (\nabla S)_{\perp}$. Here, the transverse direction means the $+y$ direction at the instant of the electric-field peak. In Fig. 8(d), we show the transverse velocity distributions for the ionized wave function at the peak of the electric field calculated by the QCS model, in comparison with the result by the CCSFA. One can see that the peak of the transverse velocity distributions are the same for those two models. The most probable transverse velocity for the 400-nm laser field is larger than that for the 800-nm laser field, indicating a stronger nonadiabatic effect for the tunneling ionization in the 400-nm laser field [57]. One can further see that the transverse velocity distributions of the ionized electron at the peak of the electric field from the QCS are narrower than those from the CCSFA and show some sharp features on one side. Those result from the effect of the HK propagator on the electron when the electron-ion distance is larger than the classical tunnel exit position, similar to the effect of the quantum potential on the electron in Bohmian mechanics [28].

IV. CONCLUSION

In summary, we have developed a QCS approach to explore the electron dynamics in both tunneling ionization and multiphoton ionization. The QCS method transforms each Bohmian trajectory to a bunch of Gaussian wave packets in analogy to optical diffraction, enabling a combination of Bohmian trajectory and HK propagator during the wave packet propagation. Using this method, we have reproduced most of the relevant features in the PMDs of the attoclock in both tunneling and multiphoton ionization regimes. By selecting the electron trajectories released within one laser cycle, we remove the intercycle interference pattern from the PMDs and obtain sub-laser-cycle electron dynamics during the ionization

process. We find that the average crossing time of the electron calculated by the QCS agrees with that using the quasiclassical method in the tunneling ionization regime while it differs from the quasiclassical result in the multiphoton ionization regime. We have also obtained the electron position and the transverse velocity distributions near the tunnel exit by back-propagating the ionized electron wave packets semiclassically to the instant of the peak electric field. We hope the QCS can be employed to study strong-field processes of more complex targets in the near future, such as molecules and solids.

ACKNOWLEDGMENTS

This work is supported by the National Key Research and Development Program of China (Grant No. 2019YFA0308300) and the National Natural Science Foundation of China (Grants No. 12021004 and No. 62275085). The computation was completed in the HPC Platform of Huazhong University of Science and Technology. This work is also dedicated to the 40th birthday of School of Physics, Huazhong University of Science and Technology.

-
- [1] P. Agostini, F. Fabre, G. Mainfray, G. Petite, and N. K. Rahman, *Phys. Rev. Lett.* **42**, 1127 (1979).
- [2] P. B. Corkum, *Phys. Rev. Lett.* **71**, 1994 (1993).
- [3] D. Shafir, H. Soifer, B. D. Bruner, M. Dagan, Y. Mairesse, S. Patchkovskii, M. Y. Ivanov, O. Smirnova, and N. Dudovich, *Nature (London)* **485**, 343 (2012).
- [4] D. N. Fittinghoff, P. R. Bolton, B. Chang, and K. C. Kulander, *Phys. Rev. Lett.* **69**, 2642 (1992).
- [5] B. Walker, B. Sheehy, L. F. DiMauro, P. Agostini, K. J. Schafer, and K. C. Kulander, *Phys. Rev. Lett.* **73**, 1227 (1994).
- [6] L. V. Keldysh, *Sov. Phys. JETP* **20**, 1307 (1965); F. H. M. Faisal, *J. Phys. B: Atom. Mol. Phys.* **6**, 553 (1973); H. R. Reiss, *Phys. Rev. A* **22**, 1786 (1980).
- [7] W. Becker, F. Grasbon, R. Kopold, D. B. Milošević, G. G. Paulus, and H. Walther, *Adv. At. Mol. Opt. Phys.* **48**, 35 (2002).
- [8] D. B. Milošević, G. G. Paulus, D. Bauer, and W. Becker, *J. Phys. B* **39**, R203 (2006).
- [9] X. Xie, S. Roither, D. Kartashov, E. Persson, D. G. Arbó, L. Zhang, S. Gräfe, M. S. Schöffler, J. Burgdörfer, A. Baltuška, and M. Kitzler, *Phys. Rev. Lett.* **108**, 193004 (2012).
- [10] S. P. Goreslavski, G. G. Paulus, S. V. Popruzhenko, and N. I. Shvetsov-Shilovski, *Phys. Rev. Lett.* **93**, 233002 (2004).
- [11] C. Figueira de Morisson Faria and A. S. Maxwell, *Rep. Prog. Phys.* **83**, 034401 (2020).
- [12] B. HuP, J. Liu, and S. G. Chen, *Phys. Lett. A* **236**, 533 (1997).
- [13] S. V. Popruzhenko and D. Bauer, *J. Mod. Opt.* **55**, 2573 (2008).
- [14] S. V. Popruzhenko, G. G. Paulus, and D. Bauer, *Phys. Rev. A* **77**, 053409 (2008).
- [15] T. M. Yan, S. V. Popruzhenko, M. J. J. Vrakking, and D. Bauer, *Phys. Rev. Lett.* **105**, 253002 (2010).
- [16] M. Li, J.-W. Geng, H. Liu, Y. Deng, C. Wu, L.-Y. Peng, Q. Gong, and Y. Liu, *Phys. Rev. Lett.* **112**, 113002 (2014).
- [17] N. I. Shvetsov-Shilovski, M. Lein, L. B. Madsen, E. Räsänen, C. Lemell, J. Burgdörfer, D. G. Arbó, and K. Tórkési, *Phys. Rev. A* **94**, 013415 (2016).
- [18] X.-Y. Lai, C. Poli, H. Schomerus, and C. Figueira de Morisson Faria, *Phys. Rev. A* **92**, 043407 (2015).
- [19] N. I. Shvetsov-Shilovski, D. Dimitrovski, and L. B. Madsen, *Phys. Rev. A* **87**, 013427 (2013).
- [20] N. Camus, E. Yakaboylu, L. Fechner, M. Klaiber, M. Laux, Y. Mi, K. Z. Hatsagortsyan, T. Pfeifer, C. H. Keitel, and R. Moshhammer, *Phys. Rev. Lett.* **119**, 023201 (2017).
- [21] N. Teeny, E. Yakaboylu, H. Bauke, and C. H. Keitel, *Phys. Rev. Lett.* **116**, 063003 (2016).
- [22] N. Teeny, C. H. Keitel, and H. Bauke, *Phys. Rev. A* **94**, 022104 (2016).
- [23] X. Wang, J. Tian, and J. H. Eberly, *Phys. Rev. Lett.* **110**, 243001 (2013).
- [24] W. Xie, J. Yan, M. Li, C. Cao, K. Guo, Y. Zhou, and P. Lu, *Phys. Rev. Lett.* **127**, 263202 (2021).
- [25] A. N. Pfeiffer, C. Cirelli, M. Smolarski, D. Dimitrovski, M. Abu-samha, L. B. Madsen, and U. Keller, *Nat. Phys.* **8**, 76 (2012).
- [26] M. Klaiber, K. Z. Hatsagortsyan, and C. H. Keitel, *Phys. Rev. Lett.* **114**, 083001 (2015).
- [27] N. Douguet and K. Bartschat, *Phys. Rev. A* **97**, 013402 (2018).
- [28] W. Xie, M. Li, Y. Zhou, and P. Lu, *Phys. Rev. A* **105**, 013119 (2022).
- [29] J. Wu, B. B. Augstein, and C. Figueira de Morisson Faria, *Phys. Rev. A* **88**, 063416 (2013).
- [30] M. F. Herman and E. Kluk, *Chem. Phys.* **91**, 27 (1984).
- [31] E. Kluk, M. F. Herman, and H. L. Davis, *J. Chem. Phys.* **84**, 326 (1986).
- [32] M. F. Herman, *J. Chem. Phys.* **85**, 2069 (1986).
- [33] K. G. Kay, *J. Chem. Phys.* **100**, 4377 (1994).
- [34] K. G. Kay, *J. Chem. Phys.* **100**, 4432 (1994).
- [35] K. G. Kay, *J. Chem. Phys.* **101**, 2250 (1994).
- [36] F. Grossmann, *Phys. Rev. Lett.* **85**, 903 (2000).
- [37] J. C. Burant and V. S. Batista, *J. Chem. Phys.* **116**, 2748 (2002).
- [38] S. Zhang and E. Pollak, *Phys. Rev. Lett.* **91**, 190201 (2003).
- [39] G. van de Sand and J. M. Rost, *Phys. Rev. A* **62**, 053403 (2000).
- [40] G. van de Sand and J. M. Rost, *Phys. Rev. Lett.* **83**, 524 (1999).
- [41] C. Zagoya, J. Wu, M. Ronto, D. Shalashilin, and C. Figueira de Morisson Faria, *New J. Phys.* **16**, 103040 (2014).
- [42] M. Spanner, *Phys. Rev. Lett.* **90**, 233005 (2003).
- [43] M. D. Feit, J. A. Fleck, Jr., and A. Steiger, *J. Comput. Phys.* **47**, 412 (1982).
- [44] M. Protopapas, C. H. Keitel, and P. L. Knight, *Rep. Prog. Phys.* **60**, 389 (1997).
- [45] S. Chelkowski, C. Foisys, and A. D. Bandrauk, *Phys. Rev. A* **57**, 1176 (1998).
- [46] X. M. Tong, K. Hino, and N. Toshima, *Phys. Rev. A* **74**, 031405(R) (2006).
- [47] D. Bohm, *Phys. Rev.* **85**, 166 (1952); **85**, 180 (1952).
- [48] S. Garashchuk and V. A. Rassolov, *Chem. Phys. Lett.* **364**, 562 (2002).
- [49] S. Garashchuk and V. A. Rassolov, *J. Chem. Phys.* **118**, 2482 (2003).
- [50] J. H. Van Vleck, *Proc. Natl. Acad. Sci. USA* **14**, 178 (1928); M. C. Gutzwiller, *J. Math. Phys.* **8**, 1979 (1967).
- [51] L. Torlina and O. Smirnova, *Phys. Rev. A* **86**, 043408 (2012); L. Torlina, M. Ivanov, Z. B. Walters, and O. Smirnova, *ibid.* **86**, 043409 (2012).

- [52] D. G. Arbó, S. Yoshida, E. Persson, K. I. Dimitriou, and J. Burgdörfer, *Phys. Rev. Lett.* **96**, 143003 (2006).
- [53] L. Torlina, F. Morales, J. Kaushal, I. Ivanov, A. Kheifets, A. Zielinski, A. Scrinzi, H. G. Muller, S. Sukiasyan, M. Ivanov, and O. Smirnova, *Nat. Phys.* **11**, 503 (2015).
- [54] H. Ni, U. Saalman, and J. M. Rost, *Phys. Rev. Lett.* **117**, 023002 (2016).
- [55] A. W. Bray, S. Eckart, and A. S. Kheifets, *Phys. Rev. Lett.* **121**, 123201 (2018).
- [56] V. V. Serov, A. W. Bray, and A. S. Kheifets, *Phys. Rev. A* **99**, 063428 (2019).
- [57] D. Trabert, N. Anders, S. Brennecke, M. S. Schöffler, T. Jahnke, L. P. H. Schmidt, M. Kunitski, M. Lein, R. Dörner, and S. Eckart, *Phys. Rev. Lett.* **127**, 273201 (2021).
- [58] H. Xie, M. Li, S. Luo, Y. Li, Y. Zhou, W. Cao, and P. Lu, *Phys. Rev. A* **96**, 063421 (2017).
- [59] X. Xie, *Phys. Rev. Lett.* **114**, 173003 (2015).
- [60] R. Landauer and T. Martin, *Rev. Mod. Phys.* **66**, 217 (1994).
- [61] N. Yamada, *Phys. Rev. Lett.* **93**, 170401 (2004).
- [62] D. Sokolovski and L. M. Baskin, *Phys. Rev. A* **36**, 4604 (1987).
- [63] D. Sokolovski, S. Brouard, and J. N. L. Connor, *Phys. Rev. A* **50**, 1240 (1994).
- [64] A. S. Landsman, M. Weger, J. Maurer, R. Boge, A. Ludwig, S. Heuser, C. Cirelli, L. Gallmann, and U. Keller, *Optica* **1**, 343 (2014).
- [65] P. Eckle, A. N. Pfeiffer, C. Cirelli, A. Staudte, R. Dörner, H. G. Muller, M. Büttiker, and U. Keller, *Science* **322**, 1525 (2008).